doi:10.1038/nature11096

Spectroscopic redshifts of CDF-N X-ray sources

We have taken a recent compilation[13] as our main source of spectroscopic redshifts. These redshifts are given to two decimal places, but the majority of them originate from earlier studies, so we have in most cases obtained more precise redshifts by tracing them back to the original publications. Where there is a significant discrepancy ($> 2\%$) between a spectroscopic redshift in our main source and that given in earlier literature, we have adopted the redshift from our main source[13]. We have utilised a number of spectroscopic redshifts which are not listed there. The redshifts and literature references for these cases are given in Table S1.

Effect of redshift incompleteness

While we have restricted our study to objects within the CDF-N which have optical spectroscopic identifications and redshifts to ensure fidelity in redshifts and luminosities, we must examine whether the limited spectroscopic completeness (64%) has any effect on our results. A large fraction of the X-ray sources within the CDF-N have photometric redshifts (i.e. redshifts estimated by comparing photometry in a number of bands to that expected from galaxy template spectra as a function of redshift) in the same compilation that we use for our spectroscopic redshifts[13]. Although these photometric redshifts are of low accuracy and reliability compared to the spectroscopic redshifts, they raise the redshift completeness of the 2–8 keV X-ray sources to 87%, and so offer a good test as to whether the spectroscopic completeness has a significant influence on our results. Table S2 gives statistics equivalent to those shown in Table 1 of the main paper, but with the photometric redshifts included. As found for the spectroscopic-only sample, no AGN more luminous than 10^{44} erg s^{-1} are associated with 250 μm sources.

We can be further reassured that our main result is not affected by the spectroscopic incompleteness by looking specifically at the identification statistics of those 2–8 keV X-ray sources which are associated with 250 μm sources. A total of 33 2–8 keV X-ray sources are associated with 250 μm sources, of which 27 are spectroscopically identified. The spectroscopically-identified fraction of these sources is thus 82%, higher than the 2–8 keV source population as a whole. For the 6 sources without spectroscopic redshifts, Fig. S1 shows the tracks of X-ray luminosity as a function of redshift. We can see that with respect to the $1 < z < 3$,

Source number in X-ray catalogue[12]	Spectroscopic redshift	Reference
91	0.294	[30]
121	0.520	[31]
152	0.540	[14]
191	0.952	[14]
196	0.680	[32]
205	0.943	[14]
220	4.420	[33]
223	2.724	[34]
243	0.557	[35]
266	1.2258	[14]
287	2.737	[14]
292	0.497	[36]
317	1.760	[14]
342	0.518	[30]
377	3.1569	[14]
412	1.1435	[14]
423	2.365	[14]
441	0.634	[31]
443	0.033	[30]
470	0.231	[31]

Table S1: Spectroscopic redshifts which do not come from our main source[13] and references to the literature in which these redshifts are published.

10^{43} erg s^{-1}< L_X < 10^{45} erg s^{-1} region which is well sampled by the X-ray and submillimetre surveys, sources 31, 37 and 431 from the X-ray catalogue[12] have $L_X < 10^{44}$ erg s^{-1} for all $1 < z < 3$. The tracks for sources 107, 221 and 406 all cross the upper rectangle corresponding to $1 < z < 3$, 10^{44} erg s^{-1}< L_X < 10^{45} erg s^{-1}, and so should be examined in more detail. The track for source 221 only enters this rectangle for a tiny redshift interval ($2.94 < z < 3.0$). Although our main redshift compilation[13] does not give a photometric redshift for source 221, a photometric redshift of 1.9 is found elsewhere in the literature[37], in which case it has $L_X < 10^{44}$ erg s^{-1} in keeping with the other 250 μm-detected AGN. Source 107 is within 6 arcsec of the same 250 μm source as a brighter X-ray source (source 109), which has a spectroscopic redshift of 2.58. The brighter X-ray source is closer to the 250 μm source position than source 107, and source extraction using X-ray and 24 μm positions as priors[25] does not recover significant 250 μm emission for source 107, leaving some doubt about the reality of the association. Source 107 has a photometric redshift of 1.15, but could be physically associated with source 109 at $z = 2.58$ given that they are only separated by 2.7 arcsec. It can be seen from Fig. S1 that whichever of the two redshifts is adopted for source 107, it has L_X between 10^{43} erg s^{-1} and 10^{44} erg s^{-1}, and hence if the association

Region of (z,L) parameter space	Number of AGN	Number of AGN associated with 250 μm sources	Expected number of spurious associations	Fraction of AGN associated with 250 μm sources
all z, $10^{42} < L_X < 10^{45}$ erg s^{-1}	248	27	2.8	11$\pm$2 ($\pm$4) %
$1 < z < 3$, $10^{43} < L_X < 10^{44}$ erg s^{-1}	61	12	0.7	20$\pm$6 ($^{+12}_{-9}$) %
$1 < z < 3$, $10^{44} < L_X < 10^{45}$ erg s^{-1}	25	0	0.3	< 4 (< 11) %

Table S2: 250 μm detection statistics in the various parts of parameter space when AGN with photometric redshifts are included as well as those with spectroscopic redshifts. The first row corresponds to the full AGN luminosity and redshift parameter space in the CDF-N, while the second and third rows correspond to the regions enclosed within the blue dashed lines in Fig. 1.

of source 107 and the 250 μm source is real, it too has $L_X < 10^{44}$ erg s^{-1}, in keeping with the other 250 μm-detected AGN. Finally, we come to source 406, which is the brightest of the six X-ray sources. From the track in Fig. S1, it appears the most likely of the six to be found within the $1 < z < 3$, 10^{44} erg s^{-1}$< L_X < 10^{45}$ erg s^{-1} region of our survey. This source is extremely faint in the optical, with an R-band magnitude of 27.8[31], and there are no estimates of photometric redshift available in the literature. The association of this X-ray source with the 250 μm source must be regarded with some doubt, however, because it is located just 5.5 arcsec to the south of a brighter 24 μm and radio source which is closer to the 250 μm position. Source extraction using X-ray and 24 μm positions as priors[25] detects source 406 only at the 3σ level. Nonetheless, this source does represent the single example of an X-ray source, potentially associated with a 250 μm source, with a reasonable likelihood of lying within the $1 < z < 3$, $L_X > 10^{44}$ erg s^{-1} region. Equally, it may fall within the $1 < z < 3$, $L_X < 10^{44}$ erg s^{-1} region. To summarise, it appears that the sources without spectroscopic redshifts are likely to harbour at most one object within the redshift range $1 < z < 3$, which has $L_X > 10^{44}$ erg s^{-1}.

Effect of X-ray absorption

X-rays in the 2–8 keV band can penetrate considerable column densities of material, but column densities $> 10^{23}$cm^{-2} can lead to significant attenuation of the X-ray flux. Conceivably, the different 250 μm detection rates for AGN above and below 10^{44} erg s^{-1} could be a consequence of X-ray absorption, if 250 μm-luminous AGN are systematically more heavily absorbed than AGN which are not detected at 250 μm. X-rays in the 0.5–2 keV band are absorbed more easily than those in the 2–8 keV band which was used to select our X-ray sample, and hence the hardness ratio of 2–8 keV / 0.5–2 keV X-rays is a crude but effective estimator of the degree of X-ray absorption.

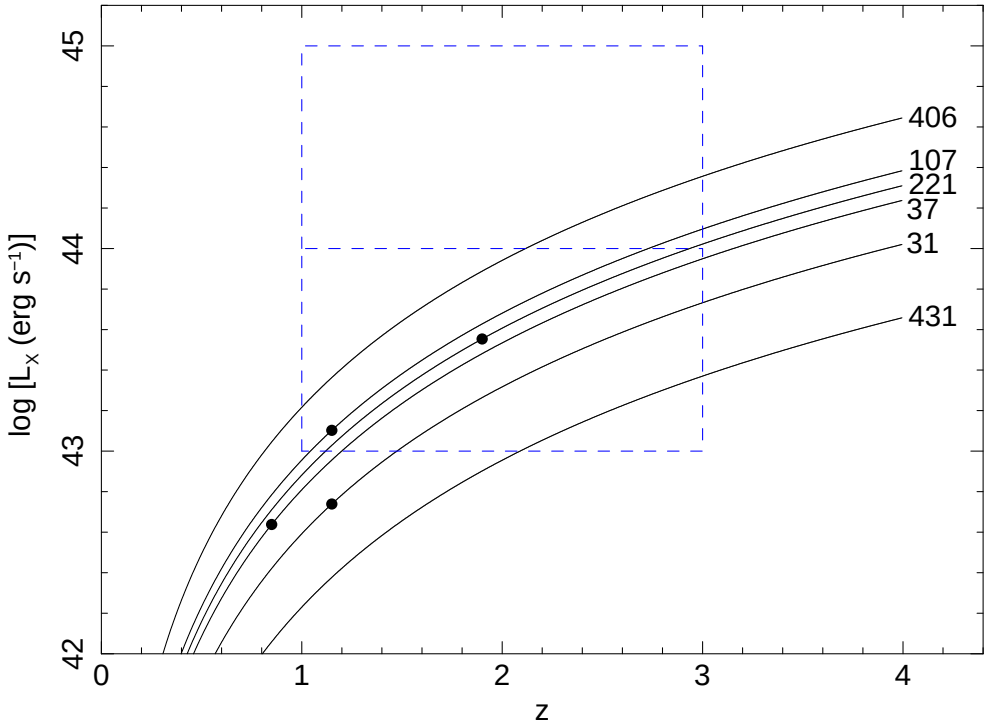

Figure S1: 2–8 keV X-ray luminosities as a function of redshift for 2–8 keV X-ray sources which are associated with 250 μm sources and which do not have spectroscopic redshifts. The bold dots indicate photometric redshfits, where available. The blue dashed rectangle delimits the luminosity decades above and below 10^{44} erg s^{-1} in the $1 < z < 3$ redshift range as in Fig. 1. Error bars correspond to 68% confidence.

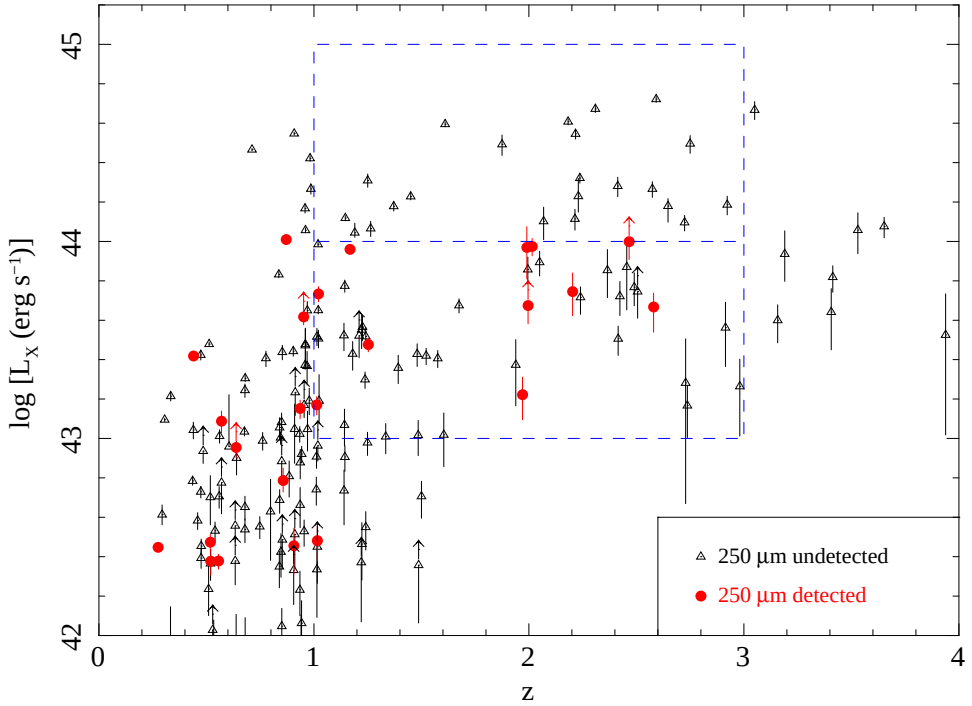

Figure S2: 2–8 keV X-ray luminosities as a function of redshift after correction for absorption. AGN with lower-limit hardness ratios have absorption-corrected luminosities with unconstrained upper bounds, and these are shown as upward pointing arrows. The blue dashed rectangle delimits the luminosity decades above and below 10^{44} erg s^{-1} in the $1 < z < 3$ redshift range as in Fig. 1. Error bars correspond to 68% confidence.

For each 2–8 keV X-ray source, we used the Portable Interactive Multi-Mission Simulator (PIMMS; http://heasarc.nasa.gov/docs/software/tools/pimms.html) to convert from hardness ratios to spectral indices and column densites. The intrinsic spectra of faint AGN without absorption are power laws of the form $S_\nu \propto \nu^{-\alpha}$ with a mean $\alpha = 0.9$, and an rms scatter in α of 0.2[15]. We took a hardness ratio corresponding to $\alpha = 0.5$ (2σ from the mean) as the threshold beyond which we considered sources as absorbed. For absorbed sources, we used PIMMS to estimate the column density, assuming an intrinsic spectral index $\alpha = 0.9$. PIMMS was then used to calculate the expected degree of attenuation to the observed 2–8 keV X-rays from the column density estimate. The X-ray luminosities were then adjusted accordingly. Where only a lower limit to the hardness ratio is available (due to the faintness of the object in the 0.5–2 keV X-ray band), the luminosity correction corresponding to the lower limit is applied.

Fig. S2 shows how Fig. 1 would be affected by the absorption corrections. More than half of the 250 μm-detected AGN increase in luminosity when the absorption corrections are applied, but on the whole these corrections are quite modest, with the majority amounting to less than 40% change in luminosity. None of the 250 μm-detected AGN move into the $1 < z < 3$, $10^{44}\,\mathrm{erg\ s^{-1}} < L_X < 10^{45}\,\mathrm{erg\ s^{-1}}$ region. Although several of the 250 μm-detected AGN move close to the $10^{44}\,\mathrm{erg\ s^{-1}}$ boundary, and the absorption corrections for two of the 250 μm-detected AGN are lower limits such that they may have intrinsic luminosities $> 10^{44}\,\mathrm{erg\ s^{-1}}$, the essential characteristic of Fig. 1, the low 250 μm detection rate above $10^{44}\,\mathrm{erg\ s^{-1}}$, persists.

The fraction of absorbed AGN is known to depend on luminosity[38] such that absorption is less common in the most luminous AGN. In light of this interdependency between luminosity and absorption, we have also examined the 250 μm detection rate of AGN with $1 < z < 3$ and $10^{43}\ \mathrm{erg\ s^{-1}} < L_X < 10^{45}\ \mathrm{erg\ s^{-1}}$ as a function of X-ray absorption rather than X-ray luminosity. Dividing the sample into absorbed and unabsorbed sources using the hardness-ratio criterion given above, we have 9 absorbed and 2 unabsorbed AGN detected at 250 μm, and 27 each of absorbed and unabsorbed sources which are not detected at 250 μm. Applying a Fisher's exact test, we find that the difference in 250 μm detection rate between absorbed and unabsorbed sources is significant at a little less than 95%. We can reduce the influence of the intrinsic anti-correlation between absorption and luminosity within the sample under test by excluding the sources with X-ray luminosities above $10^{44}\ \mathrm{erg\ s^{-1}}$. We then have 9 absorbed and 2 unabsorbed sources detected at 250 μm, with 19 absorbed and 14 unabsorbed sources

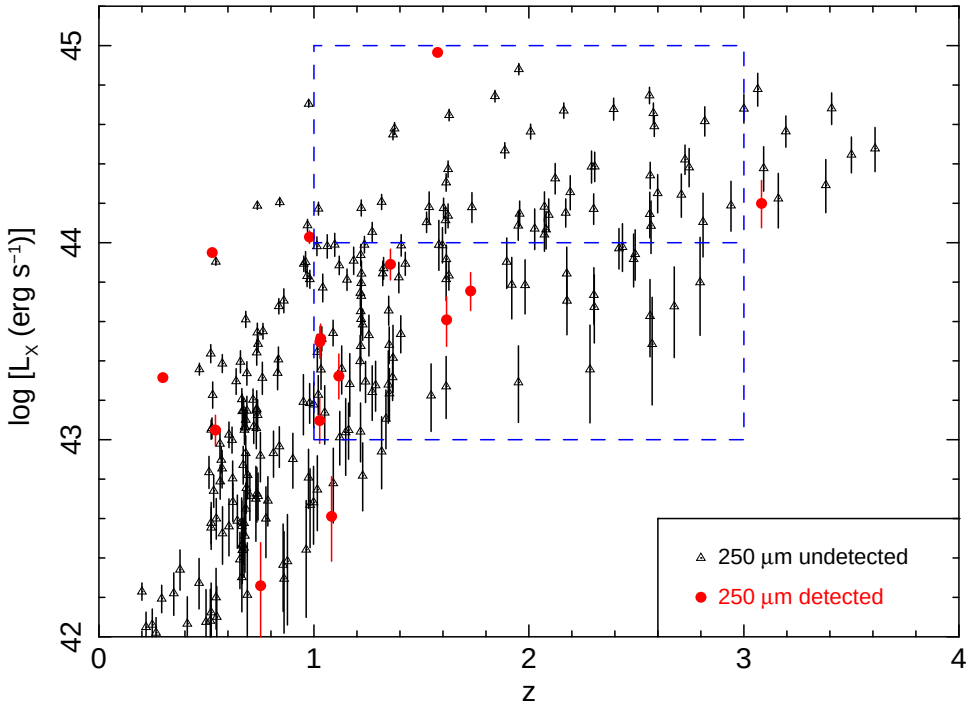

Figure S3: 2–8 keV X-ray luminosities as a function of redshift for the ECDF-S field. The blue dashed rectangle delimits the luminosity decades above and below 10^{44} erg s^{-1} in the $1 < z < 3$ redshift range as in Fig. 1. Error bars correspond to 68% confidence.

undetected at 250 μm. Applying the Fisher's test, the statistical significance at which the 250 μm detection rate depends on X-ray absorption drops to 90%. Hence, whereas we can demonstrate that the 250 μm detection rate depends on X-ray luminosity, we can not state with such confidence that the 250 μm detection rate depends on X-ray absorption.

Verification in the Extended Chandra Deep Field South

We have verified that the main result of this work, the paucity of 250 μm-detections amongst X-ray-luminous AGN, is reproduced in the Extended Chandra Deep Field South (ECDF-S), which is a larger field than the CDF-N, containing a larger sample of AGN with $L_X > 10^{44}$ erg s^{-1}. We used the published X-ray catalogue[39] and spectroscopic redshifts[40]. The SPIRE observations of the ECDF-S are shallower than those of CDF-N, but nonetheless are limited primarily by confusion. As with CDF-N, we have adopted a detection threshold of 18 mJy at 250 μm, and cross-correlated the X-ray and submillimetre catalogues with a matching radius of 6 arcseconds. The 250 μm detections in the ECDF-S (z, L) plane are shown in Figure S3, analogous to Fig. 1 of the main article. Of 49 sources with $1 < z < 3$ and $L_X > 10^{44}$ erg s^{-1}, only 1 is detected at 250 μm, confirming

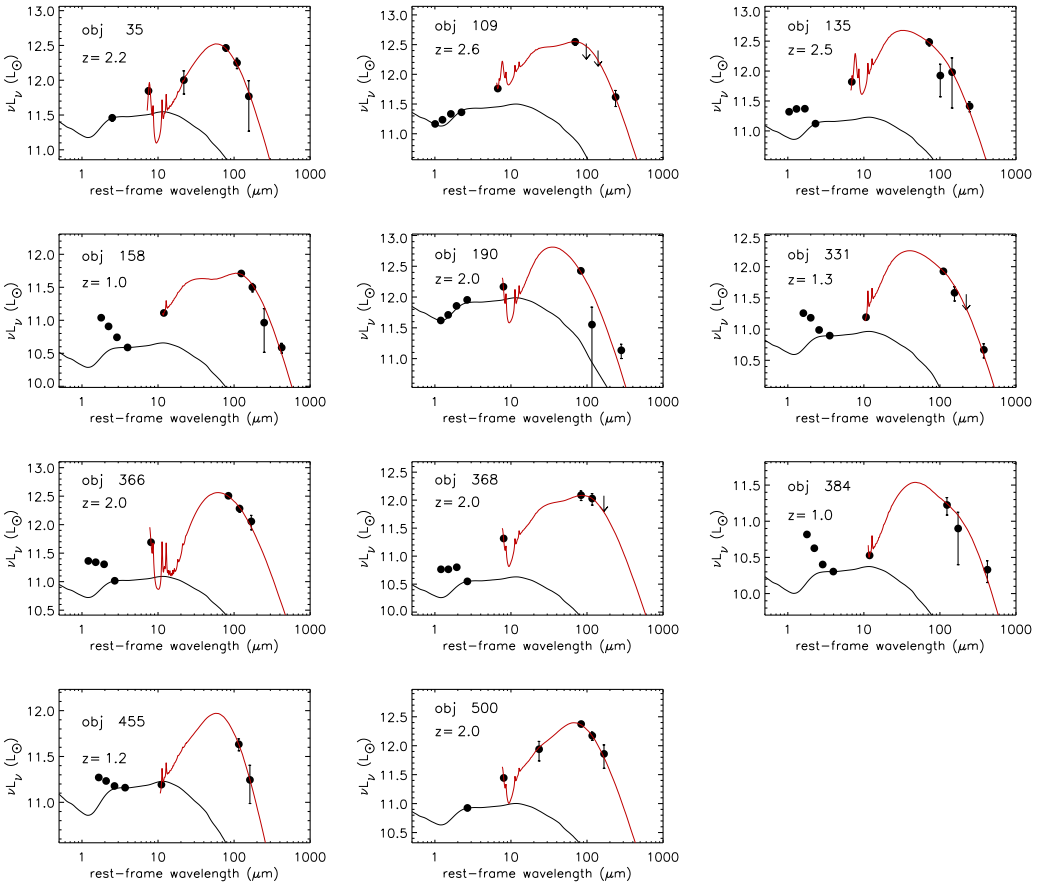

Figure S4: Infrared spectral energy distributions of 250 μm-detected AGN with $1 < z < 3$ and 10^{43} erg s^{-1} $< L_X < 10^{44}$ erg s^{-1}, based on SPIRE and *Spitzer* data. We included 850 μm and 1.3 mm photometry from ground-based telescopes where available[41;42]. The black datapoints are the measured photometry, and the red lines show the star-forming model templates[26] which best fit the data at 24 μm and longward. The black lines show AGN templates[43], normalised in the mid-IR to estimate the AGN contribution[28]. Each panel is labelled with the identity of the object in the X-ray catalogue[12].

the low detection rate obtained in the CDF-N.

Infrared spectral energy distributions of 250 μm-detected AGN

The spectral energy distributions and best fit models for the AGN associated with 250 μm sources with $1 < z < 3$ and 10^{43} erg s^{-1} $< L_X < 10^{44}$ erg s^{-1}, are shown in Fig. S4

Obtaining the average star formation rates through stacking

The average star formation rates shown in Fig. 2 were obtained by averaging the far-infrared luminosities

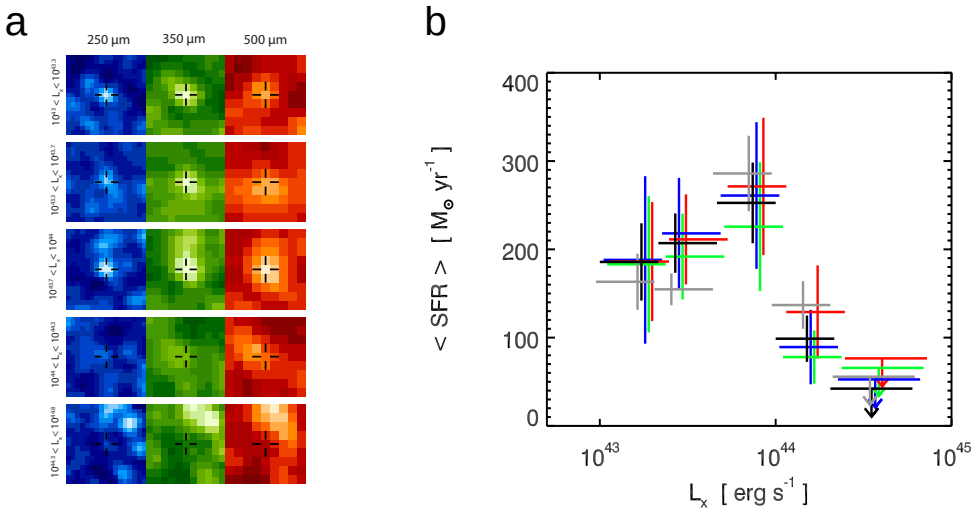

Figure S5: (a) Stacked 250, 350 and 500 μm SPIRE images of AGN in the five luminosity bins used for Fig. 2. The images are arranged in increasing wavelength from left to right and decreasing X-ray luminosity from bottom to top. (b) Star formation rates obtained from the stacked fluxes and median redshifts (grey) compared to the star formation rates obtained from stacking the luminosities as in Fig. 2 (black). The blue, green and red points show the star formation rates obtained in a similar fashion to the black points, but in these cases using only one of the SPIRE bands to determine the luminosities prior to averaging. Blue, green and red correspond to 250, 350 and 500μm bands. The points have been offset slightly in the horizontal direction to aid clarity.

of the AGN to account for the different redshifts of the different AGN. It is more common in stacking analyses to average the fluxes of the objects, and then to use the average flux and the median redshift of the sample to infer an average luminosity. Here we examine how the results would change if we used this latter method rather than stacking directly in luminosity. Fig. S5 shows the star formation rates obtained by the two different methods. The two methods give consistent results, and in both cases the average star formation rates are significantly higher for AGN with $\log L_X < 10^{44}$ erg s^{-1} than for AGN with $\log L_X > 10^{44}$ erg s^{-1}. We have also examined how the star formation rates would differ if only one of the SPIRE bands were used, instead of all three, to determine the luminosities. For each of the SPIRE bands, we derived a luminosity for each source by normalising a 30 K grey-body in the rest frame to the SPIRE flux and multiplying by $4\pi D_L^2$, before averaging the luminosities in each bin. The star formation rates so derived from the three SPIRE bands are shown in Fig. S5, and are consistent with each other as well as those shown in Fig. 2.

References

[30] Barger A.J., et al., X-Ray, Optical, and Infrared Imaging and Spectral Properties of the 1 Ms Chandra Deep Field North Sources. *Astron. J.*, 124, 1839-1885 (2002)

[31] Barger A.J., et al., Optical and Infrared Properties of the 2 Ms Chandra Deep Field North X-Ray Sources. *Astron. J.*, 126, 632-665 (2003)

[32] Cohen J.G., et al., Redshift Clustering in the Hubble Deep Field. *Astrophys. J.*, 471, L5-L9 (1996)

[33] Waddington I., et al., NICMOS Imaging of the Dusty Microjansky Radio Source VLA J123642+621331 at z=4.424. *Astrophys. J.*, 525, L77-L80 (1999)

[34] Barger A.J., et al., Supermassive Black Hole Accretion History Inferred from a Large Sample of Chandra Hard X-Ray Sources. *Astron. J.*, 122, 2177-2189 (2001)

[35] Wirth G.D., et al., The Team Keck Treasury Redshift Survey of the GOODS-North Field. *Astron. J.*, 127, 3121-3136 (2004)

[36] Cowie L.L., et al., A Large Sample of Spectroscopic Redshifts in the ACS-GOODS Region of the Hubble Deep Field North. *Astron. J.*, 127, 3137-3145 (2004)

[37] Donley J.L., Rieke G.H., Perez-Gonzalez P.G., Rigby J.R., Alonso-Herrero A., Spitzer Power-Law Active Galactic Nucleus Candidates in the Chandra Deep Field-North. *Astrophys. J.*, 660, 167-190 (2007)

[38] Della Ceca R., et al., The cosmological properties of AGN in the XMM-Newton Hard Bright Survey. *Astron. Astrophys.*, 487, 119-130 (2008)

[39] Lehmer B.D., et al., The Extended Chandra Deep Field-South Survey: Chandra Point-Source Catalogs. *Astrophys. J. Suppl.*, 161, 21-40 (2005)

[40] Silverman J.D., et al., The Extended Chandra Deep Field-South Survey: Optical Spectroscopy of Faint X-ray Sources with the VLT and Keck. *Astrophys. J. Suppl.*, 191, 124-142 (2010)

[41] Chapman S., Blain A.W., Smail I., Ivison R.J., A redshift survey of the submillimetre galaxy population. *Astrophys. J.*, 622, 772-796 (2005)

[42] Tacconi L.J., et al., High-resolution millimetre imaging of submillimeter galaxies. *Astrophys. J.*, 640, 228-240

[43] Elvis M., et al., Atlas of quasar energy distributions. *Astrophys. J. Suppl.*, 95, 1-68 (1994)